
**STRENGTH
AND PLASTICITY**

Effect of Melt-In and Key-Hole Modes on the Structure and Mechanical Properties of AISI 430 Steel Welded Using Plasma Transfer Arc Welding¹

Tanju Teker*

Faculty of Engineering, Department of Metallurgical and Materials Engineering, University of Adiyaman, Adiyaman, 02040 Turkey

**e-mail: tteker@adiyaman.edu.tr*

Received October 23, 2016; in final form, January 15, 2018

Abstract—In this study, AISI 430 stainless steel couple 10 mm thick were welded in the butt position by melt-in and key-hole plasma transfer arc welding (PTAW) processes without using any filler wire addition and pre-treatment. Welded joints were manufactured choosing a constant nozzle diameter (2.4 mm), welding speed (0.01 m/min), shielding gas flow rate (25 L/min), two different plasma gas flow rates (0.8 and 1.2 L/min), three different welding currents in melt-in PTAW process (80, 85 and 90 A), and three current intensities of the key-hole PTAW process (120, 125, and 130 A). In order to determine the microstructural changes that occurred, the interface regions of the welded samples were examined by scanning electron microscopy (SEM), optic microscopy (OM), X-ray diffraction (XRD) after PTAW. Microhardness and V-notch impact tests were applied to determine the mechanical properties of the welded samples. In addition, fracture surface were examined by SEM after impact tests.

Keywords: plasma transfer arc welding, melt-in, key-hole, AISI430 stainless steel

DOI: 10.1134/S0031918X18070116

1. INTRODUCTION

The welding technique used in this research is plasma transfer arc welding (PTAW), in which the electric arc generated between a non-consumable tungsten electrode and the working piece is constrained using a copper nozzle with a small opening at the tip. By forcing the plasma gas and arc through a constricted orifice, the torch delivers a high concentration of energy to a small area, giving higher welding speeds and producing welds with high penetration/width ratios, thus limiting the heat-affected zone (HAZ) dimensions. For these reasons PTAW is a very useful technique for welding stainless steels.

The PTAW process is essentially an extension of gas tungsten-arc welding (GTAW) [1, 2]. The energy density and gas velocity and momentum in the plasma arc are high. Three operating modes can be produced by varying the nozzle diameter and the plasma gas flow rate: Microplasma operates between 0.1 and 15 A, melt-in plasma operates between 15 and 100 A, and key-hole plasma operates above 100 A. As with electron beam and laser beam welding, PTAW exhibits a deep-weld effect. The low cost and easily operated process gives key-hole PTAW important advantages over the other high-energy-density-beam welding

processes. Therefore, PTAW is widely used to weld stainless steel, high-nickel alloys, carbon steel, copper, copper/nickel alloys, titanium alloys, and aluminum and magnesium alloys. PTAW has found applications on the welding of structural steels, automobiles, airplanes, rockets, pressure vessels, large diameter pipes, space shuttles and possibly on welding in space [3–7].

Ferritic stainless steels (FSS) constitute approximately one-half of the AISI type 400 series stainless steels. These steels contain 10.5 to 30% of Cr along with other alloying elements, notably molybdenum. FSS are noted for their excellent stress corrosion cracking resistance and good resistance to pitting and crevice corrosion in chloride environments. While these alloys have useful properties in the wrought condition, welding is known to reduce toughness, ductility, and corrosion resistance because of grain coarsening and formation of martensite [8, 9].

Teker [10] reported the effect of austenitic interlayer in key-hole PTAW of AISI 430 FSS couples. The results show that the austenitic stainless steel interlayer increased the impact strength of welding. Ureña et al. [11] investigated optimum welding conditions (welding intensity and travel speed) for butt joints of 2205 duplex stainless steel sheets using PTAW. Minimum net energy input for proper operative and metallurgical weldabilities is studied using two different

¹ The article is published in the original.

Table 1. The chemical compositions and weight percentages of test material

Chemical compositions, wt %								
Alloy	Fe	Cr	C	Ni	Si	Mo	S	Mn
AISI 430	Bal.	16.02	0.048	0.022	0.44	0.016	0.002	0.610

Table 2. The process parameters used in plasma transfer arc welding

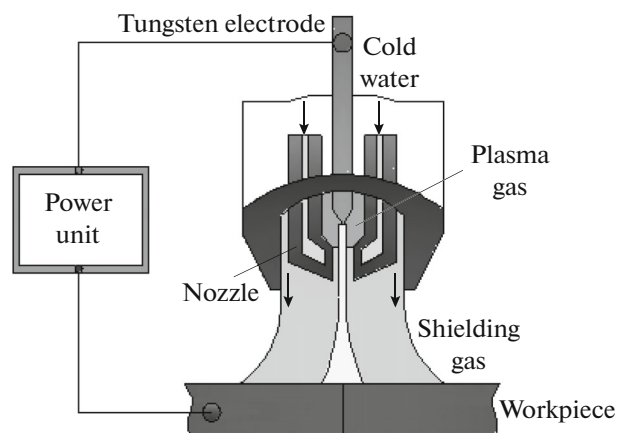
Sample no.	Current, A	Plasma gas flow rate, L/min	Shielding gas flow rate, L/min	Welding speed, m/min	Nozzle diameter, mm	Selected process
S1	80	0.8	25	0.01	2.4	Melt-in
S2	85	0.8	25	0.01	2.4	Melt-in
S3	90	0.8	25	0.01	2.4	Melt-in
S4	120	1.2	25	0.01	2.4	Key-hole
S5	125	1.2	25	0.01	2.4	Key-hole
S6	130	1.2	25	0.01	2.4	Key-hole

welding modes: the melt-in or conduction mode and the key-hole mode. Welds produced by key-hole PTAW had higher penetration/width ratios than welds produced in the melt-in mode. Migiakis et al. [12] investigated the effect of key-hole PTAW on microstructure and mechanical properties of UNS S32760 super duplex stainless steel. Kahraman et al. [13] examined the effect of welding current on the PTAW of pure titanium. Titanium plates were joined successfully by plasma arc welding method at various welding currents without filler metal using a single pass metal. The welded joint strength was found to be at least as much as that of the base metal when suitable welding current was used. Correa et al. [14] declared the weldability of iron-based powder metal materials by using pulsed PTAW process. Iron-based powder metal alloys can be successfully joined by pulsed KPAW process

without filler metal. No excessive hardening was observed in the welded zone and HAZ of the powder metal Fe and Fe–Ni alloys.

In another paper, Taban [15] studied the effect of PTAW on the toughness of UNS 32750 super duplex stainless steel. Superduplex grade is possible by PAW without filler metal. The impact results showed that both welds exhibited good weld metal and HAZ toughness properties at subzero temperatures such as down to -60°C .

In the present study, AISI 430 FSS plate couples of 10 mm thickness were welded in the butt position without using any a filler wire addition and pretreatment using the melt-in and key-hole PTAW techniques. The aim of this study was to investigate the weldability of similar materials, and the effect of process parameters on the penetration depth, microstructure, and mechanical behaviors.

**Fig. 1.** The operating principle of plasma transfer arc welding process.

2. EXPERIMENTAL

AISI 430 ferritic stainless steel couple of $100 \times 50 \times 10 \text{ mm}^3$ was welded in the butt position without any filler wire addition and pretreatment by using the melt-in and key-hole PTAW processes. The chemical compositions and weight percentages of test materials is shown in Table 1. Welds were produced by using PTAW equipment in which the torch was fixed to an automatic mobile system to control both the travel speed and the nozzle/workpiece distance. Pure argon gas was used both as for shielding and the plasma gas. A schematic representation of the PTAW system is shown in Fig. 1, and the process parameters are given in Table 2. For metallographic examination, the welded samples were cut transversely through the bond by using a low-speed saw. The cross-section

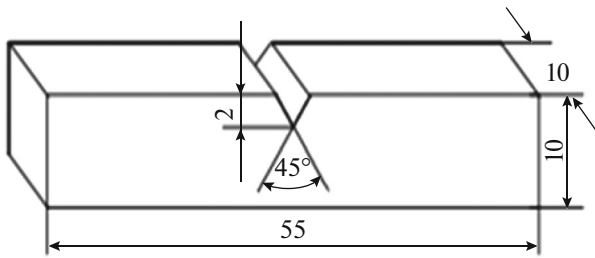


Fig. 2. Dimension of the V-Notch impact test sample.

areas of these joints were metallographically polished by using 3 μm of diamond paste and then cleaned by using acetone. For microstructural examination, the welded samples were etched electrolytically in a solution of 50% HCl + 30% H₂O + 20% NHO₃. The microstructure properties in the welding interface of the welded samples were investigated by optical microscope (OM), scanning electron microscope (SEM: ZEISS) devices. In order to determine the phases and compounds in samples, X-ray diffraction (XRD) analysis was performed by using an XRD-6000 equipped with a CuK α /tube, wave length of $\alpha = 1.54056 \text{ \AA}$, voltage of 40 kV, and ampere of 40 mA. The mechanical performances, such as microhardness and impact strength, were also tested. Microhardness measurements were analyzed by a Leica MHT-10 microhardness tester using a typical Vickers tip under a load of 50 g for 15 s. Impact test samples were pre-

pared at dimensions of $55 \times 10 \times 10 \text{ mm}^3$ in (Fig. 2), and then the samples were tested by using a Wolpert PW30 V-notch impact test device with a hammer of 300 J. ASTM: E23-04 guidelines were followed for preparing and testing the impact samples. The fractured surface of impacted samples was analyzed by using SEM at higher magnification to study the fracture morphology to establish the nature of the fracture.

3. RESULTS AND DISCUSSION

3.1. Macro and Microstructure Characteristics

Figures 3a, 3b show the widths of welding surfaces of samples S1, S2, and S3 welded by melt-in PTAW process by using three different welding currents (80, 85, and 90 A) and the constant nozzle orifice diameter of 2.4 mm. Figures 4a, 4b show the widths of welding surfaces of samples S4, S5, and S6 welded by key-hole PTAW process using three different welding currents (120, 125, and 130 A) and the constant nozzle orifice diameter of 2.4 mm. As it can be seen in the Figs. 3a, 3b, the widths of weld metal surfaces in the samples S1, S2 and S3 welded by melt-in PTAW process are approximately 5, 5.5, and 6 mm, and the penetration depths in the welded samples were obtained as 3, 3.5, and 4 mm, respectively. Also, as it can be seen in the Fig. 4a, b, the widths of weld metal surfaces in the samples S4, S5, and S6 welded by key-hole PTAW process are approximately 8, 8.5, and 9 mm, and the penetra-

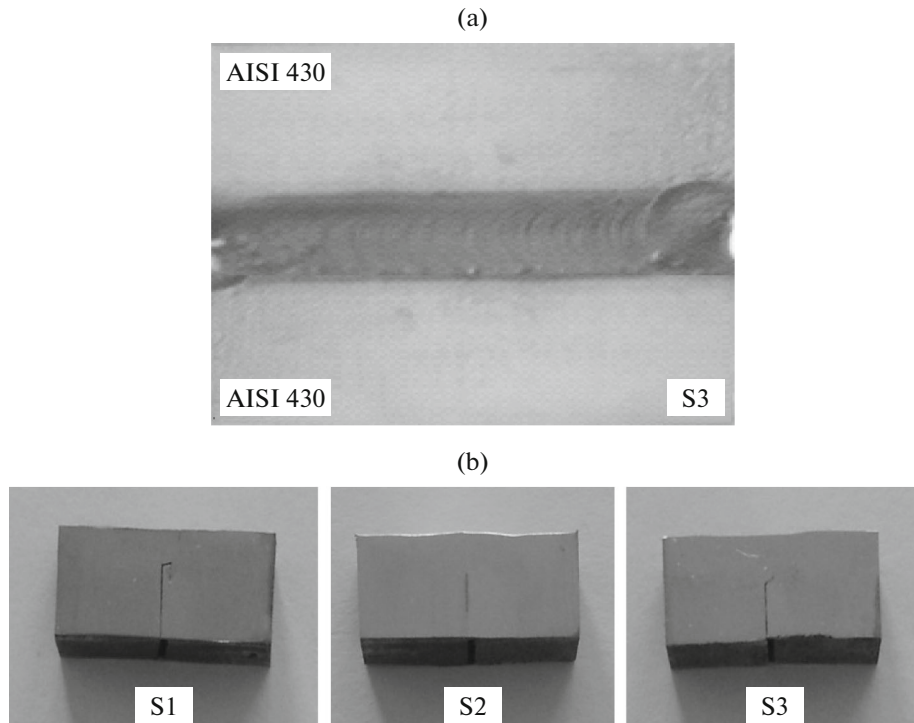


Fig. 3. The macro appearance of welded samples S1, S2, and S3. (a) Surface, (b) cross-sectional.

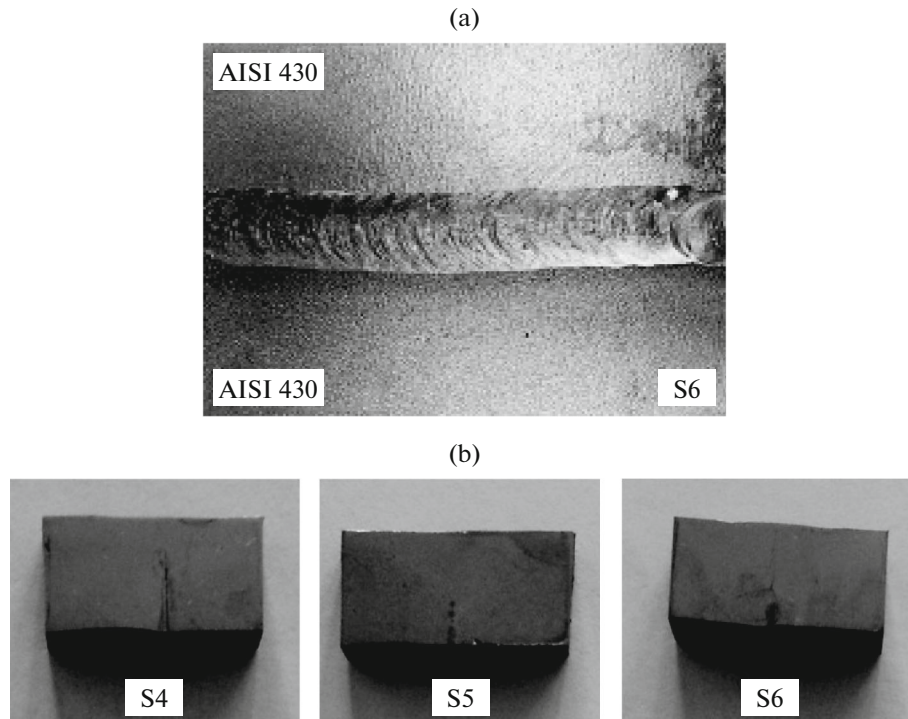


Fig. 4. The macro appearance of welded samples S4, S5, and S6; (a) surface, (b) cross-sectional.

tion depths in the welded samples have been obtained as 7, 7.5, and 8 mm, respectively. Being examined, the surface images taken from the weld face of the welded joints were observed to be basically similar and smooth with co-altitude seam structure.

Present investigations were focused on some insight into the microstructure-property relationships in the welding of the martensite, duplex, and austenite stainless steels in similar and dissimilar metal combinations. There is scarce information in the literature about the possible effect of PTAW in terms of playing connection role on similar FSS. Also, rare studies exist about weld quality features (especially mechanical behaviors, full penetration depth in one single pass) and till now the quality of such welds has not been still significantly improved. PTAW showed an alternative technique providing a better way to overcome these weld quality features. 10 mm thick, AISI 430 FSS couple was welded by melt-in and key-hole PTAW techniques without using any filler wire addition and pretreatment. The best penetration deep was obtained in keyhole PTAW.

Macroscopic studies of the cross-sections of the melt-in and key-hole PTAW joints showed that the lowest net input energy condition was insufficient in producing complete penetration. Key-hole joints, which were carried out by using the same orifice gas nozzle with a diameter of 2.4 mm, presented higher width/penetration ratios. The influence of the net

input energy (H_{net}), defined as the proportion of heat input per length reaching the work-piece, on the penetration, shape, and size of the welds has been evaluated as indicated in Eq. (1). Within this scope, the values of H_{net} were calculated, considering the plasma welding conditions (I , E , and V) together with the values of energy transfer efficiencies (η)—for both groups of welds (melt-in and key-hole). The values of η for modes melt-in and key-hole used have been typical PTAW values as reported by other authors [16] and they have given transfer efficiency ranges of 0.70–0.85 for melt-in mode and 0.85–0.95 for key-hole mode. In both cases, we have chosen an intermediate value within these ranges ($\eta_{\text{melt-in}} = 0.8$ and $\eta_{\text{key-hole}} = 0.9$).

$$Q = \eta IU/V \text{ (J/cm)}. \quad (1)$$

For purposes of comparison, Eq. (1) is valid by assuming that most of the parameters that could influence the energy losses happening between the welding source and the work piece during welding are fixed. Therefore, the mode of energy deposition (melt-in or key-hole) will be the main factor for determining the difference in the energy transfer between the two weld modes.

The existence and size of unwelded sections in the interface of the two welded metal pairs are remarkable for both welding modes (melt-in and key-hole). Depending on the increasing energy input, the size and amount of unwelded sections decreased. The

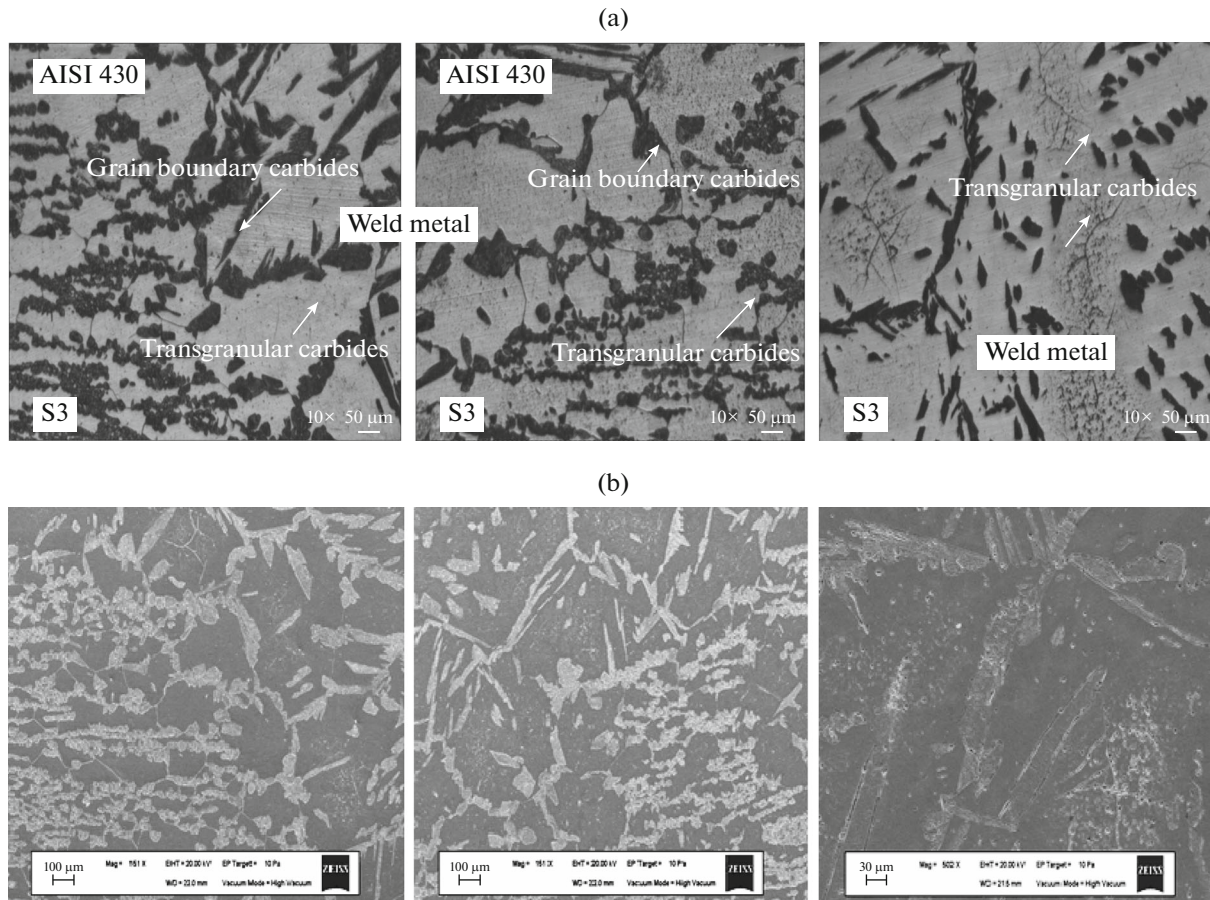


Fig. 5. (a) Optical micrograph of the weld metal and transition zone of sample S3; (b) The SEM micrographs taken from the welding interface of sample S3.

highest penetration depth was obtained for the welded joints S3 and S6. These results showed that welding current and plasma gas flow rate are important parameters in the melt-in and key-hole PTAW modes [16, 17]. As a result of welding current's increasing, the volume of welding metal expanded. The welded connections that were produced by using higher heat input reveal a characteristic cross-section profile: the key-hole profile has formed.

There were no signs of cracking in either melt-in or key-hole mode welds or the molten pool and the HAZ. So, it can be said that work piece thickness and welding conditions have no effect on the stress levels in both welding zones. Melt-in PTAW joints with medium net input energies have been characterized by narrow HAZs in the range of 5, 5.5–6 mm, however they exhibited considerable ferrite grain growth. Key-hole PTAW joints with high net input energies have been characterized by wider HAZs in the range from 6.5, 7 to 7.5 mm.

The SEM and OM micrographs of the welding interfaces of melt-in PTAW joints S1–S3 were shown

in Figs. 5a, 5b. The SEM and OM micrographs of the welding interfaces of key-hole PTAW joints S4–S6 are shown in Fig. 6a, b. By examining the microstructure images taken from the weld interface of the welded joints, the formed structures were determined to be quite similar, and no cracks or cavities were observed. The micrographs of weld metal exhibit microstructures of coarse ferrite grains with randomly distributed carbides as is seen from the results of XRD analysis. This grain growth zone influenced the subsequent epitaxial growth of the columnar ferrite grains inside the fusion pool. The inter-granular and intra-granular (pepper like) precipitations in the ferrite grain boundaries and grain inners were enhanced in the form the fusion pool, and the proportions with more energetic welding conditions were used. A two-phase ferrite plus martensite fusion zone microstructure is shown in Figs. 5 and 6. The martensite was present along the ferrite grain boundaries and is generally present as a continuous grain boundary phase. FSS welded samples exhibit fine dispersion of precipitates within the ferrite or at the ferrite-martensite boundary. A similar

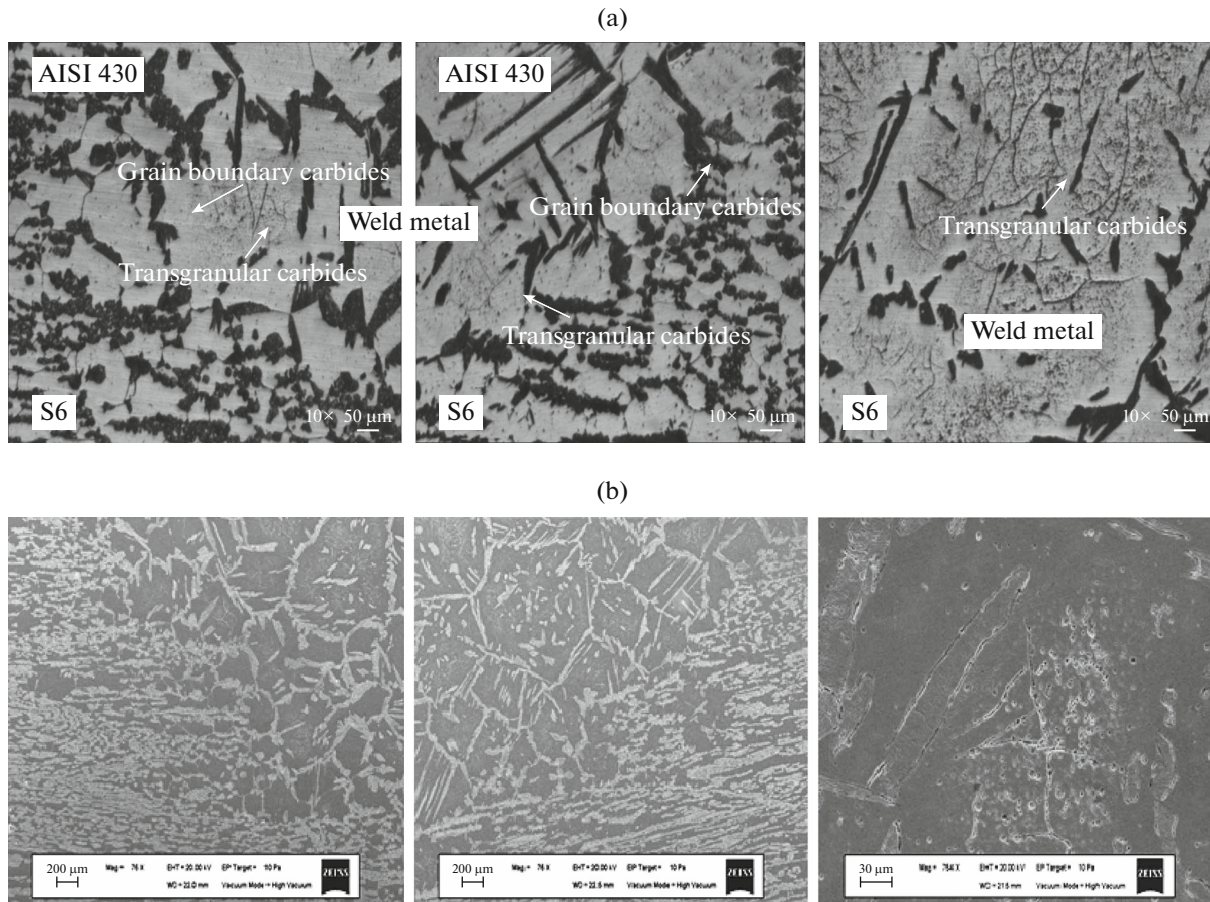


Fig. 6. (a) Optical micrograph of the weld metal and transition zone of sample S6; (b) The SEM micrographs taken from the welding interface of sample S6.

precipitation behavior was observed in the HAZ. Very fine equiaxed ferrite grains with grain boundary (of lath type) martensite were observed in the HAZ. On the HAZ side, the zone containing coarse grains, which consisted of ferrite phases and chromium carbides, also included the large amount of chromium

carbide, specifically in the intra-granular (pepper like) forms as is shown in Figs. 5 and 6.

The formation of inter-metallic phases, such as Cr_3C_2 , Cr_7C_3 , and Cr_{23}C_6 , has not been detected in these low-energy conditions. However, when the input energy was increased during key-hole PTAW, and especially when short arc distances were used, the formation of partial melting zones was detected at the base metal grain boundaries along with precipitation of inter-metallic phases. This phenomenon could be a result of a higher input energy used on these welds combined with the high thermal gradient produced during application of a high density energy welding process like PTAW in key-hole mode. Results of XRD analysis for the welded joint S6 were shown in Fig. 7. From the results of XRD analysis, Fe, Fe_3C , Cr_7C_3 , and Cr_3C_2 compounds have been seen in the melting zone (weld metal) of welded joints.

The results of the microhardness measurements performed at the cross-sections of the weld metal are seen in Fig. 8 for samples S1–S6. As it can be seen in Fig. 8, significantly similar trend was observed in the

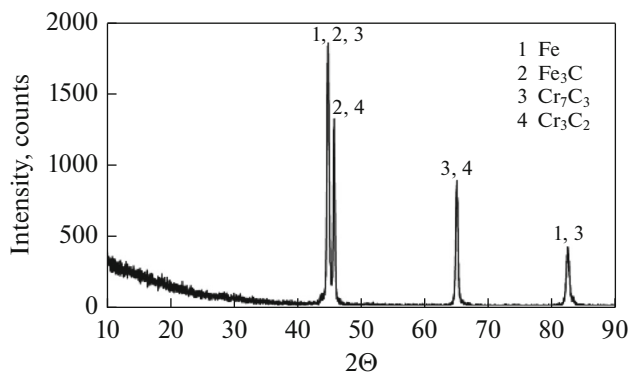


Fig. 7. The results of XRD analysis of sample S6.

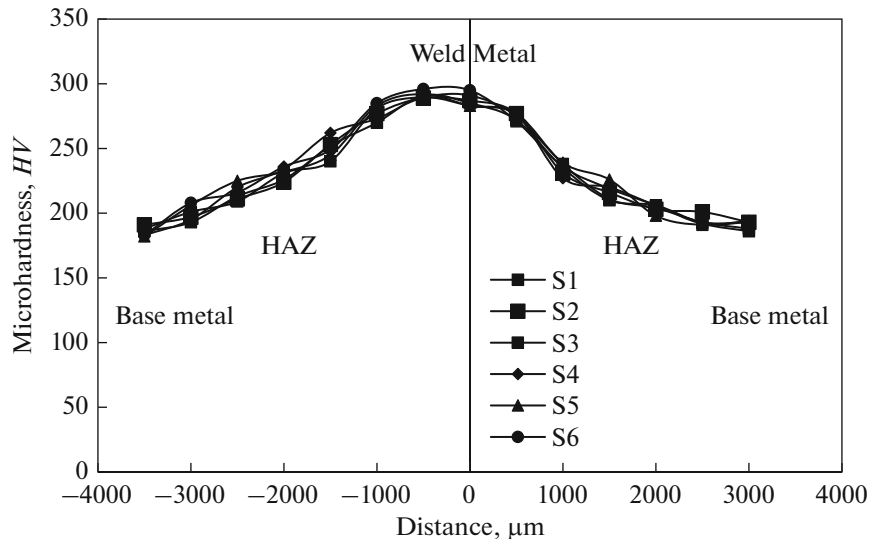


Fig. 8. Distribution of microhardness across the weld interface.

microhardness profiles of samples. As a result of formation of the chrome carbide phases and a martensitic structure in the intermediate zone, the rapid cooling increased the hardness across the weld seam zone. Based on this result, higher microhardness values were observed across the weld seam. The hardness of the welding zone was varying from 170 to 310 *HV*. With key-hole PTAW methods ensuring higher energy input, a more uniform distribution of intensive carbide formation and presence of other hard phases in the microstructure positively affected the hardness. Consequently, in case of higher heat inputs and cooling rates, the hardness of the welding zone became higher, but the hardness values rose where no carbide formed and there was no effective diffusion in the welding zone due to the formation of martensite.

Vickers hardness measurements (Fig. 8) confirmed that levels of hardening inside the fusion pools were higher than those measured in melt-in PTAW, with maximum values in the range of 170–310 *HV*, and also were higher in less energetic welding conditions. This was explained by the fact that the grain structure of these welds was fine and this increased the cooling rates. Moreover, the softening effects detected in the HAZ of melt-in welds and associated with excessive grain growth did not occur in this case; here, hardness in HAZs was intermediate between that characteristic of the fusion pool and of the parent material.

Figure 8 compares the maximum Vickers hardness measured at the center of the welds in relation to input energy, welding mode, and welding parameters. In the case of key-hole PTAW, the variation of hardness was as expected, because the increase of input energy was generally associated with an increase in welding current producing an almost linear hardening effect in the

fusion zones in correlation with higher ferrite contents. In the case of melt-in welds, the reduction of ferrite content did not produce a reduction of hardness. On the contrary, the finer microstructure of melting pools resulting from the low growth in the fusion line and the higher cooling rates determined by the steep temperature gradients has increased the hardness levels, which were generally higher because of the low net input energy.

3.2. Impact Test

The fracture energy of the welded joints were obtained respectively as S1 = 5.50 J, S2 = 6.10 J, S3 = 7 J, S4 = 9.50 J, S5 = 10.75 J, and S6 = 12 J. These results showed that the key-hole PTAW of FSS increased the fracture energy. Concurrently, depending on increasing energy input and plasma gas flow rate, an increase has been noticed in the fracture energy values of the welded joints. This can be attributed to the increasing of the penetration depth due to higher temperatures and energy density. By examining the fracture energy test values of the samples, a decrease of these values was observed depending on the decreasing welding current. Decreasing in the fracture energy values was directly associated with the penetration depth and the presence of unwelded zones. It is known that the presence and size of a unwelded zone would create a notch effect and have an impact on the fracture behavior of the V-notch impact tests. The fracture of the broken samples formed on AISI 430 side due to the formation of a martensitic structure and grain growth. In general, the toughness and ductility of FSS welds were reported to be low due to carbide precipitations and large grain size of the

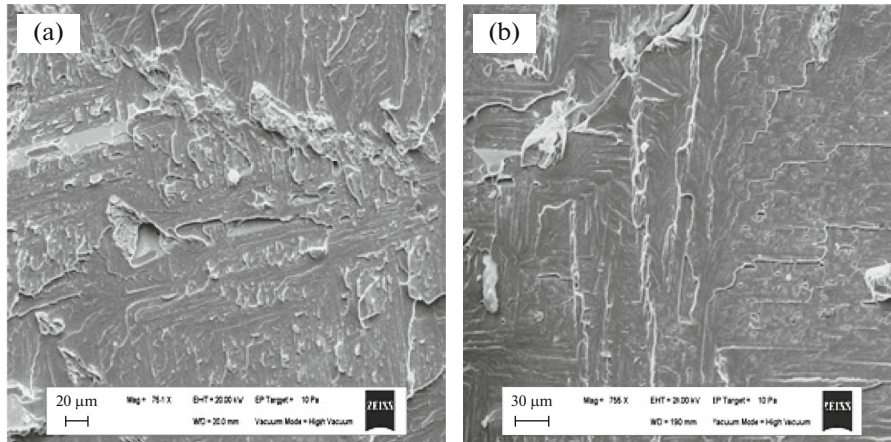


Fig. 9. SEM micrographs of fracture surfaces after notch impact test of welded sample S6.

fusion zone of AISI 430 FSS. The welding heat leads to grain coarsening in the HAZ and in the weld metal of FSS, because they solidify directly from liquid to ferrite phase without any intermediate transformation phase.

3.3. Fractography

Figure 9 shows the images of fracture surfaces resulting from the impact test of the welded joints of sample S6. As can be seen in the figure, fracture occurred in AISI 430 FSS side widely and it was observed that the broken grains had a crystalline fish backed appearance. The samples display a brittle fracture mechanism. For FSS, the fracture morphology was an intergranular crack, which was peculiar to brittle fracture, and it was reported that HAZ and the welding metal had excessive grain coarsening [18].

4. CONCLUSIONS

In this study, microstructure and mechanical properties of AISI 430 FSS welded using melt-in and key-hole PTAW modes were investigated. From this investigation the following important conclusions were derived:

(1) 10 mm thick, AISI 430 FSS couple was successfully welded by melt-in and key-hole PTAW technique in single pass without extra welding wire and pretreatment. With the PTAW modes, the best penetration deep was obtained as 4 mm in the melt-in mode and 8 mm in the key-hole mode without any filler wire addition and pretreatment.

(2) Welds produced by key-hole PTAW had higher penetration/width ratios than welds produced in the melt-in mode. HAZs of the key-hole PTAW joints underwent a softening impact associated with exces-

sive grain growth near the fusion line. This effect was not observed in melt-in welding process.

(3) If the net input energy of the key-hole PTAW increased, there was a risk of formation of brittle intermetallic phases.

(4) The highest impact strengths were obtained as 12 J by 130 A of the current intensity, in the key-hole PTAW process applied to the welded sample S6 and as 7 J by 90 A of the current intensity, in the melt-in PTAW process applied to the welded sample S3. Depending on the decrease of current intensity, a decrease was detected in the notch impact strength values because of the presence of the unwelded sections. The fracture surfaces of welded samples showed the brittle fracture mechanism.

REFERENCES

1. J. Martikainen, "Conditions for achieving high-quality welds in the plasma-arc key-hole welding of structural steels," *J. Mater. Process. Technol.* **52**, 68–75 (1995).
2. L. Yan, F. Yanhui, Z. Xinxin, and W. Chuansong, "Energy propagation in plasma arc welding with key-hole tracking," *Energy* **64**, 1044–1056 (2014).
3. B. Irving, "Plasma arc welding takes on the advanced solid rocket motor," *Weld. J.* **71**, 49–50 (1992).
4. J. Xiaoxia and S. W. Chuan, "Numerical analysis of the coupled arc-weld pool-keyhole behaviors in stationary plasma arc welding," *Int. J. Heat Mass Transfer* **84**, 839–847 (2015).
5. Y. Wang and Q. Chen, "On-line quality monitoring in plasma arc welding," *J. Mater. Process. Technol.* **120**, 270–274 (2002).
6. J. Sun, C. S. Wu, and Y. Feng, "Modeling the transient heat transfer for the controlled pulse key-holing process in plasma arc welding," *Int. J. Therm. Sci.* **50**, 1664–1671 (2011).
7. Y. M. Zhang and Y. C. Liu, "Control of dynamic key-hole welding process," *Autom.* **43**, 876–884 (2007).

8. J. C. Lippold and D. J. Kotecki, *Welding metallurgy and weldability of stainless steels* (Wiley, New York, 2005), pp. 88–135.
9. A. G. L. Azevedo, V. A. Ferraresia, and J. P. Fariasb, “Ferritic stainless steel welding with the A–TIG process,” *Weld. Int.* **24**, 571–578 (2010).
10. T. Teker, “The effect of austenitic interlayer in key-hole plasma transfer arc welding of AISI 430 ferritic stainless steel couples,” *Int. J. Adv. Manuf. Technol.* **69**, 1833–1840 (2013).
11. A. Ureña, E. Otero, M. V. Utrilla, and C. J. Múñez, “Weldability of a 2205 duplex stainless steel using plasma arc welding,” *J. Mater. Process. Technol.* **182**, 624–631 (2007).
12. K. Migiakis, N. Daniolos, and G. D. Papadimitriou, “Plasma key-hole welding of UNS S32760 super duplex stainless steel: Microstructure and mechanical properties,” *Mater. Manuf. Processes* **25**, 598–605 (2010).
13. N. Kahraman, M. Taşkın, B. Gülenç, and A. Durgutlu, “An investigation into the effect of welding current on the plasma arc welding of pure titanium,” *Kovove Mater.* **48**, 179–184 (2010).
14. E. O. Correa and S. C. Costa, “Weldability of iron-based powder metal materials using pulsed plasma arc welding process,” *J. Mater. Process. Technol.* **198**, 323–329 (2008).
15. E. Taban, “Toughness and microstructural analysis of super duplex stainless steel joined by plasma arc welding,” *J. Mater. Sci.* **43**, 4309–4315 (2008).
16. R. W. Messler, Jr., *Principles of Welding: Processes, Physics, Chemistry and Metallurgy* (Wiley, New York, 1999).
17. T. Teker and N. Ozdemir, “Weldability and joining characteristic of AISI 430/AISI 1040 steel using key-hole plasma arc welding,” *Int. J. Adv. Des. Manuf. Technol.* **63**, 117–128 (2012).
18. T. Teker and N. Ozdemir, “The effect of current intensity on penetration deep of AISI 430/AISI 1040 steel couple welded by key-hole plasma transfer arc welding process,” *Int. Iron & Steel Symp. IISS’12* (Karabük University, Karabük, Turkey, 2012), pp. 762–768.